UNIVERSIDADE ESTADUAL DE CAMPINAS
SISTEMA DE BIBLIOTECAS DA UNICAMP
REPOSITÓRIO DA PRODUÇÃO CIENTIFICA E INTELECTUAL DA UNICAMP

Versão do arquivo anexado / Version of attached file:

Versão do Editor / Published Version

Mais informações no site da editora / Further information on publisher's website:

https://www.nature.com/articles/srep06839

DOI: 10.1038/srep06839

Direitos autorais / Publisher's copyright statement:

OPEN

Compact Ag@Fe$_3$O$_4$ Core-shell Nanoparticles by Means of Single-step Thermal Decomposition Reaction

Maria Eugênia F. Brollo[1], Román López-Ruiz[1], Diego Muraca[1], Santiago J. A. Figueroa[2], Kleber R. Pirota[1] & Marcelo Knobel[1]

[1]Instituto de Física Gleb Wataghin - Universidade Estadual de Campinas (UNICAMP) 13083-970 Campinas (SP) Brasil, [2]Brazilian Synchrotron Light Laboratory (LNLS)/Brazilian Center of Energy and Materials (CNPEM) CP6192, 13083-970 Campinas (SP) Brasil.

A temperature pause introduced in a simple single-step thermal decomposition of iron, with the presence of silver seeds formed in the same reaction mixture, gives rise to novel compact heterostructures: brick-like Ag@Fe$_3$O$_4$ core-shell nanoparticles. This novel method is relatively easy to implement, and could contribute to overcome the challenge of obtaining a multifunctional heteroparticle in which a noble metal is surrounded by magnetite. Structural analyses of the samples show 4 nm silver nanoparticles wrapped within compact cubic external structures of Fe oxide, with curious rectangular shape. The magnetic properties indicate a near superparamagnetic like behavior with a weak hysteresis at room temperature. The value of the anisotropy involved makes these particles candidates to potential applications in nanomedicine.

N anotechnology presents a vertiginous and stimulating growth owing to a vast number of potential applications. In medicine, for example, it is possible to envisage a strong improvement in the efficiency of the magnetic resonance imaging or in the development of non-conventional diagnostics or therapies[1–4]. The pace of development of the area is strongly dependent on the improvement of synthesis routes, which would allow to produce, in a controlled way, new materials capable to act in the intracellular environment[5,6]. On the other hand, the new nanomaterials exhibit physical properties different from their bulk analogues, fact that brings about new challenges in fundamental science[7–10].

The possibility of building new nanostructures by mixing noble metals and magnetic nanoparticles (NPs) opens a wide spectrum of desirable synergistic and complementary effects[11]. One of the challenges is the conjunction of these two dissimilar materials in a controlled way[12]. Thus, great efforts have been made on synthetic routes to command the bonding of the heteroparticle, resulting in core-shell, dimer, composite or flower structures[13–17].

Silver NPs have been applied as a broad spectrum and highly effective bactericide[18,19]. The antibacterial mechanism is associated to the release of silver ions[20]. For medical applications, an Ag@Fe$_3$O$_4$ core-shell structure allows one to add a magnetic functionality to silver properties. Such nanostructure could lead to interesting advances to solve the lack of biocompatibility of silver, eliminating its contact with tissues (iron oxide can be considered biocompatible, at least up to the mg/ml range)[21]. However, an intriguing behavior was observed on Ag@Fe$_3$O$_4$ NPs: its bactericidal efficiency is stronger than Ag-Fe$_2$O$_3$ heterodimers or plain Ag[22]. A possible explanation of this finding is that the amorphous thin porous oxide shell facilitates the release of silver ions from an unprotected silver surface in comparison to organic-wrapped silver NPs. In contrast to this kind of thin and porous oxide shells that result from the coalescence of a flower-like structure (see references 16 and 17 for a magnetite oxide shell) in this work, a larger shell-to-core ratio Ag@Fe$_3$O$_4$ NPs were synthesized. These NPs have a rather thick and compact cubic structure shell. It is expected that this compact magnetite capping will help to hinder the diffusion of silver ions to the surroundings, increasing the biocompatibility.

In this letter, we describe a temperature-paused single-step synthetic route that was developed to produce novel Ag@Fe$_3$O$_4$ compact core-shell nanostructures. These nanoparticles are formed by a silver nucleus wrapped by a compact magnetite shell. Owing to the curious rectangular shape, we denote these particles as brick-like nanoparticles (BLNs). In order to help the understanding of the structure formation as well as to present to the interested community a complete characterization of their physical properties, the morphology and crystalline

structure were studied by means of transmission electron microscopy (TEM), X-ray diffraction (XRD) and X-ray absorption spectroscopies: X-ray absorption near edge spectra (XANES) and extended X-ray absorption fine structure (EXAFS). The magnetic characterization was performed by conventional SQUID magnetometry.

Results

Synthesis. Usually, the so-called Ag-Fe$_3$O$_4$ core-shell NPs reported in the scientific literature are, in fact, combined NPs which form dimer or flower-like combinations[23]. They are synthesized using a conventional two-steps protocol in which an iron oxide is produced by thermal decomposition on previously synthesized Ag seeds[24-25]. We developed a novel single-step protocol, in order to reduce manipulation between the steps and facilitate the synthesis control. In this case, the Ag seeds are formed in the same reaction mixture, just before the iron oxide formation. The thermal decomposition of the Fe$_3$O$_4$ precursor occurs on a silver colloid formed in the same reaction mixture by the addition of AgNO$_3$ salt. The iron precursor in the form of Fe(III) acetylacetonate complex (3 mmol), a diol reduction agent 1,2-hexadecanediol (1 mmol), a mixture of surfactants composed by oleylamine and oleic acid (12:3 mmol) and a silver salt AgNO$_3$ (1 mmol) were added on benzyl-ether (boiling point of 298°C) at room temperature on a three-neck round-bottom flask mounted on a temperature-controlled reflux system. The reaction mixture was magnetically stirred on Ar inert atmosphere without vacuum application.

The temperature was increased in a controlled way following the scheme shown in Figure 1. Usually, in the conventional two-steps protocol, a temperature pause is introduced before the reflux temperature to ensure the reagent solution and proper homogeneity. In our recent works, we have introduced this stop at relative low temperatures, typically 80–100°C[23,25]. The pause introduced in the present single-step protocol has a different purpose: it is done at 200°C, in order to separate the growth of silver (zone 1) from the proper thermal decomposition of the iron precursor (zone 2). Thus, the role of the temperature pause is essentially to divide the Ag and the iron oxide production inside a single reaction, avoiding the necessity of

manipulation and the time consuming gap between steps. If the protocol is performed without the pause, it results in the well-known non-homogeneous core-shell NPs provided vacuum is applied[16,17]. However, when the pause is introduced, the results are completely different.

Morphology and structure. Figure 1 shows TEM images of the particles obtained by the single-step reaction. At the images, Ag is in dark contrast, while lighter structures correspond to magnetite. Only two types of structures were observed (values in volume fractions): 85.5% of BLNs and 14.5% of plain Fe$_3$O$_4$ nanoparticles. Within each single BLN, approximately 99% of the volume corresponds to the magnetite shell, while just 1% to the silver core volume. The amount of conventional structures such as flower-like or dimer nanoparticles was negligible, in fact, less than 1%. It is worth noticing that the magnetite shell presents an unexpected parallelepiped geometry with average base of 13(2) nm and 15(3) nm (in case of morphological parameters, the parenthesis that represents the error in the last digit corresponds to the half width at half maximum, HWHM, extracted from the size distribution curve after counting around 40 nanoparticles). This "brick-like" structure differs from a conventionally produced core-shell structures[16,17]. The plain magnetite nanoparticles display a nearly-spherical shape with diameter of 7.0(5) nm. As seen in Figure 1 d) few isolated, nearly-spherical core-shell nanoparticles with diameter 13(3) nm were also observed. Figure 2 b) shows the size distribution of the silver core in the BLNs. The log-normal fit leads to a mean diameter of 4.7(1) nm.

Before the pause, the partial oxidation of Fe(III) to Fe(II) is visible at 70°C when the solution color changes from red to black[26]. The Ag reduction occurs in this interval and during the pause[27]. In this pause, introduced at 200°C, the iron-oleic complex, which is the intermediary product and the proper iron decomposition precursor, is formed through ligand exchange from the acetyl-acetonate complex[26]. The oleic acid is the ligand with the highest iron coordination capacity and a time (t_1) of 2 h is reported to be enough to produce the quantitative ligand exchange[26,28]. In this temperature, there is no proper decomposition to iron oxide, even in a seed-mediated reaction, i.e., in a heterogeneous medium, as in this case[26-30]. It seems to indicate that parallel to ligand exchange in the iron precursor, the
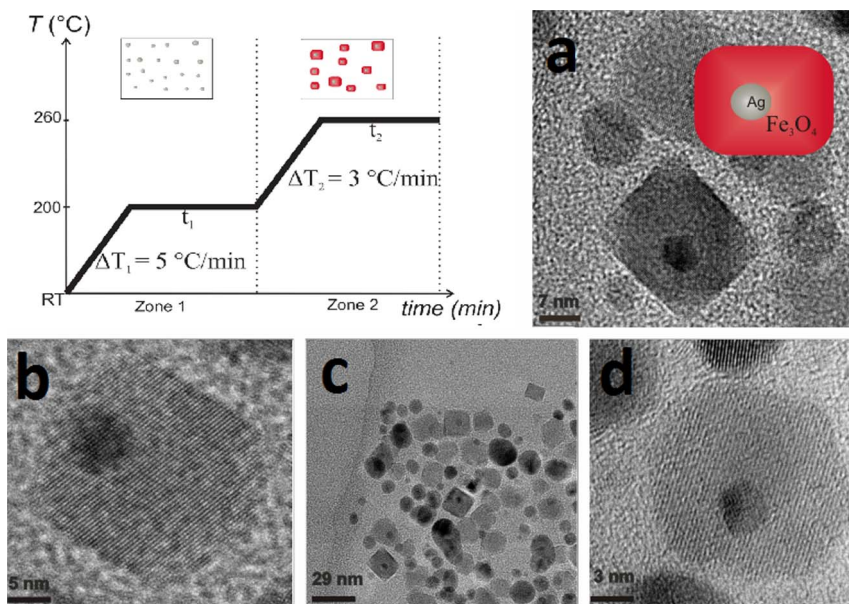

Figure 1 | Temperature profile of the temperature-paused single-step thermal decomposition synthesis. Boxes sketch the expected predominant structures for each time zone. Typically, both waiting times are 120 minutes. Images: TEM images of BLNs obtained following the temperature-paused single-step protocol. Ag corresponds to the dark contrast, while lighter particles correspond to magnetite. Plain magnetite nanoparticles which are formed are also shown in c). a) b) and d) are different amplifications of BLNs in order to understand the structure.
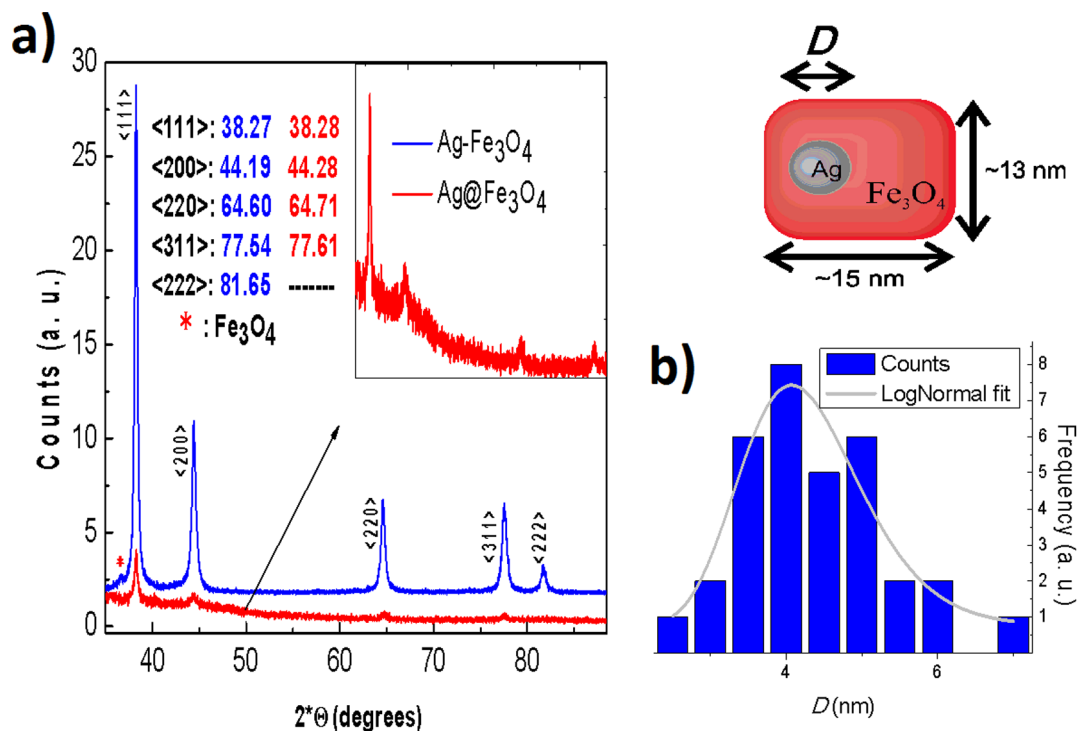
Figure 2 | (a) Conventional dimer Ag-Fe_3O_4 (blue) and BLN (red) X-ray diffraction patterns. Inset: enlargement of the X-ray diffraction pattern of the BLN sample schemed. (b) Size distribution of the Ag core within BLNs. The data was obtained from 34 counts of the TEM image analysis. The gray line corresponds to a log-normal fit.

action of surfactants (usually not present in the two-steps protocol) on the Ag seeds in this pause play a key role as steric stabilizing agent restricting the seed size[31]. The sizes in the silver core are consistent with a surfactant-mediated limitation to a second coalescence in a silver growth model proposed in the reference 32. The absence of a bimodal size distribution and polycrystalline structures also seems to corroborate this idea[32]. We have observed that pauses below 200°C reduce the quantity of BLNs. For 180°C very few BLNs were formed and for a temperature pause of 160°C there are not BLNs formation, but dimer heteroparticles are formed with bigger silver particles. It can be related to a lack of silver nuclei of appropriated size after the low temperature pause and the later simultaneous growth together to the iron oxide at higher temperatures. In fact, analogous result are observed without performing a pause, with the logical difference of the quantity of amorphous materials. For a temperature of 220°C, the size of the silver seeds are bigger and two fractions can be observed. The smaller fraction that acts as BLNs seeds and the larger one, which forms the conventional structures. The larger silver particles are characterized as a polycristals formed from silver monocristals, according to the coalescence mechanism proposed. So, taking into account the results obtained with the temperature pause variation, it can be deduced the importance of the pause in order to stabilize the silver seeds in an adequate size and 200°C as the optimal temperature. The highest temperature to perform the pause is given by the magnetite nucleation temperature between 210 and 250°C[29,30,33]. After the pause, the iron complex decomposes and a mixed valence iron oxide nucleates[26,28]. Finally, during the ramp and the reflux time (t_2) of 2 hours, growth and ripening processes occurs. The final reaction mixture exhibits a surface metallic blue color due to the presence of silver particles[16,17].

Apparently, and according to the observation of the silver BLN's seeds, there is a restriction between the type of structure that is formed and the silver size. Thus, the silver seed is not tunable at least in a wide range of values. In the case of conventional structures produced by means of the two-step route, the diameter of the silver core was always 10 nm or larger[14,23,25]. This new configuration is probably related to a wrapping mechanism below a silver seed limit, instead of the well-known multifaceted nucleation mechanism with subsequent flower structure coalescence[14,23,25]. Our hypothesis is that the so-called silver size limitation could lead to an insulator behavior, owing to quantum finite-size effects[7,8]. In such case, when the magnetite nucleates on the Ag surface, a charge density on the interface plane is induced. In the case of a small, poorly conductive (due to the possible separation of the energy electronic levels) silver nanoparticles, the surface polarization would facilitate the subsequent magnetite growth all over the silver surface, forming a compact core-shell structure. On the other hand, in the case of bigger conducting silver NPs, the charge density induced by the magnetite nucleation would be compensated by the movement of the free electrons, creating planes with a shortage or an excess of charge[34]. As a consequence, only certain planes are susceptible to nucleate, giving rise to dimer or flower structures, previously reported for the two-steps protocol[34].

Figure 2 shows X-ray diffraction patterns of the crystallographic silver planes of BLNs and a sample of conventional Ag-Fe_3O_4 in dimer form. The Ag-Fe_3O_4 dimer sample was synthesized following a conventional two-step protocol for comparative purposes (see images on Figure S1). Both spectra agree qualitatively. In the case of Ag-Fe_3O_4 dimer, the peaks are sharper than those of BLN. This is probably due to a lower crystallographic ordering in a smaller Ag particle. The small shifts observed in the position of the Ag plane peaks are probably related to interface effects between the silver and the magnetite. In the BLNs, the interface area is larger, corresponding approximately to 4% of the total silver atoms. Also, if one considers the difference in sizes, the lattice constant reduction in silver could become non-negligible.

XANES and EXAFS. The oxidation state was studied through X-ray absorption near edge spectra (XANES) and extended X-ray absorption fine structure (EXAFS). A sample of plain Fe_3O_4 NPs (hereafter named as P) with well-defined cubic geometry (edges of

27(4) nm) was chosen for comparison because of its closer magnetic properties, as will be shown later (see Figure S2 for images). The Fe K-edge XANES spectra of the BLNs and iron oxide references are shown in Figure 3. XANES features at the Fe K-edge mainly resemble those corresponding to magnetite Fe_3O_4. The pre-edge energy position is compatible with a Fe(III)-Fe(II) mixture[35]. The main component of the pre-edge peaks of Fe_3O_4 arises from tetrahedral Fe^{3+} as it is observed in the first peak for both samples. The shoulder corresponds to octahedral Fe(III)–Fe(II) ions. At lower energies, the characteristic low intensity peak corresponds to hexa-coordinated Fe(II). In BLN sample, the shoulder is shifted to high energies, higher than 1.1 eV. This limb is expected in nanometric samples that contain a maghemite fraction[35,36]. The average iron oxidation state was 2.62(1) for P sample and 2.73(2) for BLN sample. The value expected for the Fe_3O_4 magnetite phase is 2.67, which reveals that most of the iron oxide phase in BLN is indeed magnetite. A small amount of maghemite phase was also observed, as expected considering the presence of a small fraction of plain nanometric magnetite (which is absent in the P sample), where the surface oxidation becomes more relevant. The peak position, which is sensitive to oxidation state, is slightly shifted to higher energies for the BLN as expected for more oxidized species (see Figure S4). The decrease in the pre-edge peak intensity reveals that the iron environment for BLN is more centrosymmetric than in P.

From Figure 3 b) it is clear that sample P presents a closer similarity to Fe_3O_4 bulk than BLN sample. The BLN sample is closer to bulk Fe_2O_3 for the first and second environments shells. This similarity between BLN and bulk Fe_2O_3 on the EXAFS measurement and the existence of small amount of maghemite phase obtained from XANES could be ascribed to the surface oxidation in the BLN and the non-negligible amount of plain magnetite nanoparticles in the sample[36].

Magnetic characterization. DC magnetic properties were measured on the BLN sample and compared with sample P, which corresponds to plain magnetite produced without introducing silver seeds. Although the size of P is bigger than the magnetic component of the BLN (see Figure S2 for images), it exhibits closer magnetic properties; namely, a similar ZFC-FC behavior, saturation magnetization and coercive field as we can see in Figure 4, which shows the zero field cooling (ZFC) and field cooling (FC) magnetization and room temperature hysteresis loops for both samples.

FC magnetization curve remains nearly constant, except between 114 and 80 K. In this range a weak temperature dependence is observed in both samples. The irreversibility temperature, obtained from the overlap of the ZFC and FC curves, is higher than room temperature. For both samples, ZFC magnetization shows, in agreement with three different regimes[37]. For a better observation, the

inset of Figure 4 a) shows the ZFC magnetization derivative, dM(ZFC)/dT. Below 50 K (zone T1) the magnetization behavior is determined by surface freezing processes. This was confirmed by the lack of shift of the dM(ZFC)/dT maximum when different fields were applied (see Figure S3). Between 50 and 120 K (zone T2) a Verwey transition (VT) occurs near to 114 K[38,39]. Typically, for bulk materials, the VT happens at $T = 120$ K. In this transition, the conductivity shows differences of two orders of magnitude and this fact is reflected on the magnetic behavior. Above 120 K (zone T3) the magnetization behavior is ascribed to a blocking temperature related to thermally-activated phenomena, T_B. A shift to lower temperatures in the dM(ZFC)/dT maximum in the case of BLN (compared to P) is ascribed to a volume-dependent anisotropy and reinforces this temperature as the blocking temperature, T_B, of the particulate system.

The observed VT temperature, slightly smaller than 120 K, suggests a non-stoichiometric magnetite. The iron deficiency δ in the magnetite determines the behavior of the VT[40]. For values of $\delta < \delta_C$, where $\delta_C \sim 0.0117$ is a critical value, the magnetite exhibits a first order phase transition, whereas for $\delta > 3\delta_C$ a second order phase transition is expected. Based on the VT temperature value, we estimate $\delta < 0.01$, consistent with a first order phase transition[41]. This δ is probably due to surface oxidation or interactions with the Ag core. The VT observed near 120 K is associated to the magnetite shell of the BLNs, because the small fraction of plain magnetite NPs in the superparamagnetic state give an irrelevant contribution to the magnetization. In this sense, the XANES and EXAFS experiments reveal the mixture of the fractions of the sample in a more evident way than the magnetic response.

Figure 4 b) shows the hysteresis loops for both samples at 300 K. The particles are close to the superparamagnetic regime, showing rather low coercive fields: $1.8(3) \times 10^3$ A/m and $2.4(3) \times 10^3$ A/m, for BLN and P, respectively. Hysteresis loops were also measured at 2 K (not shown here) where the system is magnetically blocked, leading to coercive fields of $22.8(5) \times 10^3$ A/m for BLN and $17.9(5) \times 10^3$ A/m for P. The saturation magnetization at 300 K has similar values: 37(2) Am²/kg for BLN and 38(2) Am²/kg for P.

As distances between NPs are larger than several inter-atomic distances, the presence of dipole-dipole interactions can be neglected. Considering non-interacting magnetic monodomain particles, one can estimate the anisotropy constant, K_A, from the measured blocking temperature, T_B, using the expression $T_B = K_A V / 25 k_B$, where k_B is the Boltzmann constant and V the particle volume. The magnetic volume of the core-shell particles was estimated to be $V = 2.7 \times 10^{-23}$ m³ and the blocking temperatures were considered $T_B = 175(2)$ K for BLN and $T_B = 250(2)$ K for P (maximum of the dM(ZFC)/dT magnetization in the T3 zone, extracted from the inset of Figure 4 a). One infers anisotropy constants of 2.21×10^4 J/m³ for BLN and 48×10^4 J/m³ for P, respectively.
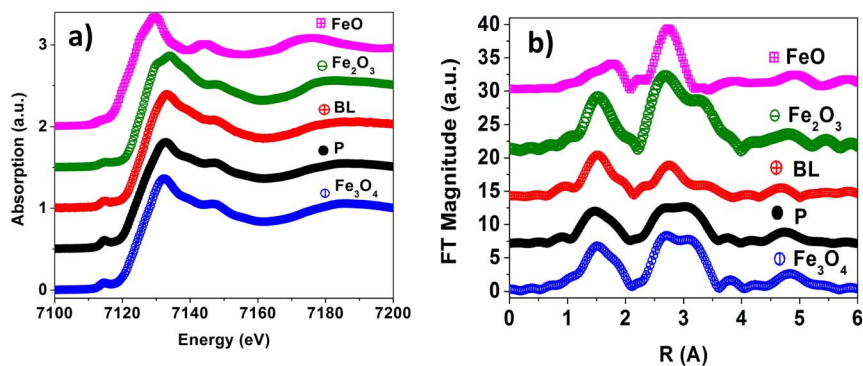

Figure 3 | (a) XANES and (b) EXAFS of BLN (red) and P (black) NPs. Also standard bulk FeO (pink), Fe_2O_3 (blue) and Fe_3O_4 (green) are shown. All spectra were obtained at room temperature.
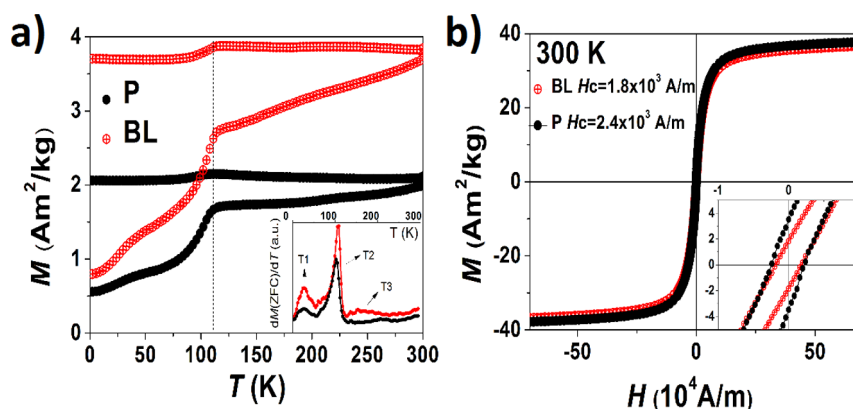
Figure 4 | (a) ZFC and FC magnetization curves for BLN (red) and P (black). Dashed line indicates the Verwey transition temperature (114 K for both samples). FC magnetization is the upper curve. Inset: first derivative of the ZFC magnetization. (b) Hysteresis loops for BLN and P samples at 300 K. Insets: zoom of the low field zone to evidence the coercivity.

Conclusion

In this paper we have presented a simple, fast and efficient synthetic route to produce novel compact core-shell structures of silver surrounded by magnetite. It consists in a parallel silver seed production in the same reaction medium of the iron thermal decomposition without vacuum application in a temperature-paused ramp. It will be widely used in the future to produce novel multifunctional materials. The studies of the size, structure and magnetic properties of the multifunctional brick-like Ag@Fe$_3$O$_4$ NPs obtained reveal them as possible candidates for advanced medical purposes. Heating efficiency studies for hyperthermia purposes are in perspective to be done. Reaction kinetics in order to understand the growing mechanisms and the subsequent synthesis control will also be studied in detail in future due to the restriction in the silver core size.

Methods

Synthesis of heterodimer Ag-Fe$_3$O$_4$ NPs (dimer for XRD comparison). They were synthesized by means of two-steps conventional protocol. The first step is the synthesis of Ag NPs. They were prepared by solution of 2 mmol of AgNO$_3$ in oleylamine (40 ml). The solution was heated to 140°C for an hour in an inert Ar atmosphere. The resulting solution was cooled to room temperature and washed four times adding 30 ml of ethanol and centrifuging at 3800 rpm for 15 minutes. The NPs are finally dispersed in a toluene/ethanol mixture 1 : 3 in volume, dried and stored in vacuum. The second step is the preparation of Ag-Fe$_3$O$_4$ dimers. The Ag NPs are used as seeds for the growth of Ag-Fe$_3$O$_4$. So, the so-called Ag NPs were added to a reaction mixture analogue to that described bellow used for the synthesis of the plain Fe$_3$O$_4$ NPs. The thermal reaction profile was also analogue. All the reagents are from Sigma-Aldrich. TEM images of the Ag-Fe$_3$O$_4$ sample in Figure S1.

Synthesis of P NPs (plain Fe3O4 for XANES/EXAFS and magnetic properties comparison). They were prepared by means of the conventional second step synthesis without adding of silver seeds. 1.059 g of Fe(acac)3 in presence of 2.58 g of 1,2-hexadecanediol and the oleic acid (1.90 ml) and oleylamine (1.97 ml) surfactant mixture were added on 20 ml of benzyl-ether. The mixture was heated to 200°C for an hour in an inert Ar atmosphere. Then, the temperature is carried to 290°C and 250°C for the 40 nm and 7 nm respectively. After 90 minutes, the solution was cooled to room temperature. The resulting NPs were washed four times by adding 30 ml of ethanol and centrifuging at 3800 rpm for 15 minutes. The NPs are finally dispersed in a toluene/ethanol mixture 1 : 3 in volume, dried and stored in vacuum. TEM images of the P sample in Figure S2.

Transmission electron microscopy (TEM) images were captured on a dried toluene dispersion of the NPs on a carbon coated copper grid. 200 keV JEOL-JEM 2100 microscope (spot size: 20–200 nm) at the Brazilian Nanotechnology National Laboratory (LNNano) that belongs to national facilities of Centro Nacional de Pesquisa em Energia e Materiais (CNPEM) was used. The images were obtained with a TV (Gatan ES500W); CCD (TVips– 16MP) cameras. Quantities, dimensions and sizes' distribution were obtained from different images over a population of 130 nanoparticles. To obtain the size function distribution a log-normal fit was performed.

X-ray diffraction (XRD) experiments were carried out on a PANalytical X'pert diffractometer. Measurements were performed using a monochromatic Cu K_a radiation (l=1.5406 Å) in 2Θ a range from 30 to 90 degrees. Data acquisition time was 5 seconds using a 0.02 degree step. Measurement samples were prepared by vacuum drying after a deposition on a cellulose film of a toluene dispersion of NPs.

Magnetic characterization was performed on dried powder samples using a commercial Quantum Design SQUID magnetometer. Magnetization temperature dependence was recorded following a ZFC-FC standard protocol. ZFC curve: the sample is cooled down from 300 K to 2 K without any magnetic field applied. Then, a small dc magnetic field (H=50 Oe) is applied and the magnetization is recorded as T increases up to 300 K; FC curve: Procedure is analogue to ZFC but now, the sample is cooled down to 2 K under an applied magnetic field (H=50 Oe). To obtain the hysteresis loops, the samples were first saturated applying a field (H=2 T) at fixed temperature and DC magnetization was measured in discrete constant fields during the field sweep.

XANES and EXAFS experiments were performed in multibunch mode on a wiggler insertion device (4 T superconducting multipole) installed at XDS beam-line on the Brazilian Synchrotron Light Laboratory (LNLS) Campinas-Brazil. Absorption spectra was obtained from few milligrams of powder mixed with boron nitride in correct proportions for have an absorption step close to one in the pellet. Transmission spectra were collected at RT using a double silicon 111 crystal monochromator, Si mirrors was used to reject higher harmonics on the beam. In order to accurately calibrate the Fe-K edge energy (taken at 7112 eV), the intensities of the incident, transmitted and through-sample beams were measured on a standard foil by three in-serie gas-filled ionization chambers. The XAFS signal X(k) was extracted using the *Iffefit* software package[42]. Pre-edge XANES fits at Fe-K edge were performed following the procedure described by Wilke et al[43].

1. Brown, M. A. Effects of the operating magnetic field on potential NMR contrast agents. *Magn. Reson. Imaging* **3**, 3 (1985).
2. Renshaw, P. F., Owen, C. S., McLaughlin, A. C., Frey, T. G. & Leigh, J. S. Ferromagnetic contrast agents: A new approach. *Magn. Reson. Med.* **3**, 217 (1986).
3. Kozissnik, B. & Dobson, J. Biomedical applications of mesoscale magnetic particles. *MRS Bulletin* **38**, 923 (2013).
4. Xu, C. & Sun, S. New forms of superparamagnetic nanoparticles for biomedical applications. *Adv. Drug Delivery Rev.* **65**, 732 (2013).
5. Bao, G., Mitragotri, S. & Tong, S. Multifunctional nanoparticles for drug delivery and molecular imaging. *Annu. Rev. Biomed. Eng.* **15**, 253 (2013).
6. Huang, K. *et al.* Size-dependent localization and penetration of ultrasmall gold nanoparticles in cancer cells, multicellular spheroids, and tumors in vivo. *ACS Nano* **6**, 4483 (2012).
7. Klitzing, K. V. The quantized Hall effect. *Rev. Mod. Phys.* **58**, 519 (1986).
8. Batlle, X. & Labarta, A. Finite-size effects in fine particles: magnetic and transport properties. *J. Phys. D: Appl. Phys.* **35**, R15 (2002).
9. Zhu, H., Zhang, S., Huang, Y. X., Wu, L. & Sun, S. Monodisperse M(x)Fe(3-x)O4 (M = Fe, Cu, Co, Mn) nanoparticles and their electrocatalysis for oxygen reduction reaction. *Nano Lett.* **13**, 2947 (2013).
10. Nguyen, T. D. Portraits of colloidal hybrid nanostructures: controlled synthesis and potential applications. *Colloids Surf. B* **103**, 326 (2013).
11. Figueroa, S. J. A., Stewart, S. J., Rueda, T., Hernando, A. & de la Presa, P. Thermal evolution of Pt-Rich FePt/Fe$_3$O$_4$ heterodimers studied using X-ray absorption near-edge spectroscopy. *J. Phys. Chem. C* **115**, 5500 (2011).
12. Zhang, L., Dou, Y. H. & Gu, H. C. Synthesis of Ag–Fe$_3$O$_4$ heterodimeric nanoparticles. *J. Colloid Interf. Sci.* **297**, 660 (2006).
13. Zhang, L., Dong, W. F. & Sun, H. B. Multifunctional superparamagnetic iron oxide nanoparticles: design, synthesis and biomedical photonic applications. *Nanoscale* **5**, 7664 (2013).
14. Wang, C., Yin, H., Dai, S. & Sun, S. A general approach to noble metal metal oxide dumbbell. Nanoparticles and their catalytic application for CO oxidation. *Chem. Mater.* **22**, 3277 (2010).

15. Yu, S. *et al.* Label-free immunosensor for the detection of kanamycin using Ag-Fe₃O₄ nanoparticles and thionine mixed graphene sheet. *Biosens. Bioelectron.* **48**, 224 (2013).

16. Huang, J. *et al.* Crystal engineering and SERS properties of Ag–Fe₃O₄ nanohybrids: from heterodimer to core–shell nanostructures. *J. Mater. Chem.* **21**, 17930 (2011).

17. Sun, L., He, J., Ren, D., An, S. & Zhang, J. Facile one-step synthesis of Ag@Fe₃O₄ core-shell nanospheres. for reproducible SERS substrates *J. Mol. Struct.* **1046**, 74 (2013).

18. Morones, J. R. *et al.* The bactericidal effect of silver nanoparticles. *Nanotechnology* **16**, 2346 (2005).

19. Xu, R. *et al.* Ag nanoparticles sensitize IR-induced killing of cancer cells. *Cell Research* **19**, 1031 (2009).

20. Sotiriou, G. A. & Pratsinis, S. E. Antibacterial activity of nanosilver ions and particles. *Environ. Sci. Technol.* **44**, 5649 (2010).

21. Seil, J. T. & Webster, T. J. *Int. J. Nanomed.* **7**, 2767 (2012).

22. Chen, Y., Gao, N. & Jiang, J. Surface matters: enhanced bactericidal property of core–shell Ag–Fe₂O₃ nanostructures to their heteromer counterparts from one-pot synthesis. *Small* **9**, 3242 (2013).

23. Muraca, D. *et al.* Influence of silver concentrations on structural and magnetic properties of Ag-Fe₃O₄ heterodimer nanoparticles. *J. Nanosci. Nanotechnol.* **12**, 6961 (2012).

24. Rockenberger, J., Scher, E. C. & Alivisatos, A. P. A new nonhydrolytic single-precursor approach to surfactant-capped nanocrystals of transition metal oxides. *J. Am. Chem. Soc.* **121**, 11595 (1999).

25. Lopes, G. *et al.* Ag-Fe₃O₄ colloidal nanoparticles: Synthesis and enhancement of magnetic properties. *J. Phys. Chem. C* **114**, 10148 (2010).

26. Roca, A. G. digital.csic.es/bitstream/10261/22726/1/Tesis_AlejandroGómez.pdf (2009) Date of access: 01/06/2014.

27. Wiley, B., Sun, Y., Mayers, B. & Xia, Y. Shape-controlled synthesis of metal nanostructures: the case of silver. *Chem. Eur. J.* **11**, 454 (2005).

28. Zhang, L., He, R. & Gu, H.-C. Synthesis and kinetic shape and size evolution of magnetic nanoparticles. *Mater. Res. Bull.* **41**, 260 (2006).

29. Sun, S. *et al.* Monodisperse MFe₂O₄ (M = Fe, Co, Mn) nanoparticles. *J. Am. Chem. Soc.* **126**, 273 (2014).

30. Roca, A. G., Morales, M. P., O'Grady, K. & Serna, C. J. Structural and magnetic properties of uniform magnetite nanoparticles prepared by high temperature decomposition of organic precursors. *Nanotechnology* **17**, 2783 (2006).

31. Polte, J. *et al.* Mechanism of colloidal silver nanoparticles: analogies and differences to the growth of gold nanoparticles. *ACS Nano* **3**, 5791 (2012).

32. Thanh, N. T. K., Maclean, N. & Mahiddine, S. Mechanisms of nucleation and growth of nanoparticles in solution. *Chem. Rev.* **114**, 7610 (2014).

33. Park, J. *et al.* Ultra-large-scale syntheses of monodisperse nanocrystals. *Nat. Mater.* **3**, 891 (2004).

34. Moscoso, O. *et al.* Physicochemical studies of complex silver–magnetite nanoheterodimers with controlled morphology. *J. Phys. Chem. C* DOI: 10.1021/jp501453m.

35. Wilke, M., Farges, F., Petit, P. E., Brown, G. E. & Martin, F. Oxidation state and coordination of Fe in minerals: An FeK-XANES spectroscopic study. *Am. Mineral.* **86**, 714 (2001).

36. Piquer, C. *et al.* Effect of nature and particle size on properties of uniform magnetite and maghemite nanoparticles. *J. Phys. Chem. C* **118**, 1332 (2014).

37. Muscas, G. *et al.* Magnetic properties of small magnetite nanocrystals. *J. Phys. Chem. C* **117**, 23378 (2013).

38. Verwey, E. J. W. Electronic conduction of magnetite. *Nature* **144**, 327 (1939).

39. Verwey, E. J. W. & Hayman, P. W. Electronic conductivity and transition point of magnetite. *Physica* **8**, 979 (1941).

40. Muxworthy, A. R. & McClelland, E. Review of the low-temperature magnetic properties of magnetite from a rock magnetic perspective. *Geophys. J. Int.* **140**, 101 (2000).

41. Shepherd, J. P., Koenitzer, J. W., Aragón, R., Spalek, J. & Honig, J. M. Heat capacity and entropy of nonstoichiometric magnetite Fe₃₍₁₋δ₎O₄: The thermodynamic nature of the Verwey transition. *Phys. Rev. B* **43**, 8461 (1991).

42. Newville, M. J. EXAFS analysis using FEFF and FEFFIT. *J. Synchrotron Radiat.* **8**, 96 (2011).

43. Wilke, M., Farges, F., Petit, P. E., Brown, G. E. & Martin, F. Oxidation state and coordination of Fe in minerals: an Fe K-XANES study. *Am. Mineral.* **86**, 714 (2001).

Acknowledgments

Author contributions

M.E.F.B. and D.M. carried out the syntheses and characterization of the nanoparticles. S.J.A.F. measured and interpreted EXAFS and XANES. R.L.R. and D.M. iniciate the project and wrote the main manuscript. K.R.P. and M.K. led the project. All authors read the manuscript, contributed to the interpretation of the data and approved the final manuscript.

Additional information